Characterization, Bioactivity and Antibacterial Properties of Copper-Based TiO₂ Bioceramic Coatings Fabricated on Titanium

Salih Durdu[ID]

Department of Industrial Engineering, Giresun University, Giresun 28200, Turkey; durdusalih@gmail.com or salih.durdu@giresun.edu.tr; Tel.: +90-4543104114

Abstract: The bioactive and anti-bacterial Cu-based bioceramic TiO₂ coatings have been fabricated on cp-Ti (Grade 2) by two-steps. These two-steps combine micro-arc oxidation (MAO) and physical vapor deposition–thermal evaporation (PVD-TE) techniques for dental implant applications. As a first step, all surfaces of cp-Ti substrate were coated by MAO technique in an alkaline electrolyte, consisting of Na_3PO_4 and KOH in de-ionized water. Then, as a second step, a copper (Cu) nano-layer with 5 nm thickness was deposited on the MAO by PVD-TE technique. Phase structure, morphology, elemental amounts, thickness, roughness and wettability of the MAO and Cu-based MAO coating surfaces were characterized by XRD (powder- and TF-XRD), SEM, EDS, eddy current device, surface profilometer and contact angle goniometer, respectively. The powder- and TF-XRD spectral analyses showed that Ti, TiO₂, anatase-TiO₂ and rutile-TiO₂ existed on the MAO and Cu-based MAO coatings' surfaces. All coatings' surfaces were porous and rough, owing to the presence of micro sparks through MAO. Furthermore, the surface morphology of Cu-based MAO was not changed. Also, the Cu-based MAO coating has more hydrophilic properties than the MAO coating. In vitro bioactivity and in vitro antibacterial properties of the coatings have been investigated by immersion in simulated body fluid (SBF) at 36.5 °C for 28 days and bacterial adhesion for gram-positive (*S. aureus*) and gram-negative (*E. coli*) bacteria, respectively. The apatite layer was formed on the MAO and Cu-based MAO surfaces at post-immersion in SBF and therefore, the bioactivity of Cu-based MAO surface was increased to the MAO surface. Also, for *S. aureus* and *E. coli*, the antibacterial properties of Cu-based MAO coatings were significantly improved compared to one of the uncoated MAO surfaces. These results suggested that Cu-based MAO coatings on cp-Ti could be a promising candidate for biomedical dental implant applications.

Keywords: micro arc oxidation (MAO); Cu nano-layer; hydrophilic surface; apatite; in vitro bioactivity; antibacterial properties

1. Introduction

Commercially pure titanium (cp-Ti) materials are preferred for dental implant applications, owing to its low density, low elastic modulus (closer to that of bone), low thermal conductivity, non-magnetic properties, high specific strength, corrosion resistance, good mechanical properties, fracture resistance and fatigue resistance and biocompatibility [1–3]. It is well-known that titanium has corrosion resistant and biocompatibility properties. These are related to the native TiO₂ layer spontaneously formed on its surface [4,5]. However, titanium implant materials cannot bond directly to the bone owing to their bio-inert nature (not bioactive), unlike bioactive ceramics such as bio-glass, glass ceramic, hydroxyapatite (HA), ZrO₂ and TiO₂ etc. [6,7]. As a result of this, the bone tissue around the implant is absorbed. This leads to slow healing and the loosening of the implant–bone interface [8]. Therefore, bioactive ceramics such as HA or TiO₂ on titanium were coated to enhance bioactivity [9,10].

TiO$_2$-based coatings have been suggested to improve corrosion resistance, bioactivity and biocompatibility of implant surfaces. They have recently received great attention for the biomedical applications owing to their more stable chemical composition [11,12]. TiO$_2$ were fabricated on cp-Ti by various surface coating methods including sol–gel [13], anodic oxidation [14], magnetron sputtering [15], electrophoretic deposition [16], acid etching [17,18], laser surface treatment [19], plasma spraying [20,21] and micro arc oxidation [22–25] etc. However, certain problems like non-homogenous structure, micro-structural control problems, micro-cracks formation, the presence of phase impurity, poor adhesion strength were observed in these methods except for MAO technique [26–28]. Thus, implant application areas of the coatings produced by these techniques are limited.

Micro-arc oxidation (MAO) is one of the most applicable methods to deposit a porous and rough bioceramic layer on valve metals such as Ti, Al, Mg, and Zr surfaces [3,29–31]. The MAO coating promotes bioactivity, biocompatibility, wear and corrosion resistance respect to other surface coating methods [32–39]. Also, the adhesion strength between the substrate/MAO coatings is excellent, owing to its in situ growth [40]. Furthermore, it is reported that the porous and rough surfaces on the implant surfaces are beneficial for the formation and Osseo-integration of new bone tissue [41]. However, the bacterial adhesion and colonization may occur on the implant surfaces under body conditions. These lead to infections at the implant site and it results in the loss of implants [42].

In order to overcome bacterial adhesion and colonization, the surface modifications of implants were increasingly carried out by numerous anti-bacterial agents such as Cu [12], Ag [43] and Zn [44] over the last few years. The Cu is one of the basic trace elements necessary for human existence. It contributes in synthesis and release of life-sustaining proteins and enzymes within the living organisms [45]. Furthermore, it actively takes part in various enzyme-based processes, for bone metabolism stimulates new vessel formation and accelerates early skin wound healing [46,47]. Therefore, it is beneficial for bone tissue formation [12]. Moreover, copper exhibits excellent antibacterial properties versus a broad spectrum of bacteria, including gram-positive and gram-negative bacteria by interfering DNA replication and disrupting cell membranes [48–50].

In particular, there have been some promising studies on the fabrication of antibacterial Cu/CuO-nanoparticles containing Cu-incorporated TiO$_2$ coatings on cp-Ti by using the MAO technique for the last five years [42,45,51–56]. Wu et al. investigated the formation and investigation of antibacterial resistances of Cu-incorporated TiO$_2$ coatings by MAO and hydrothermal treatment (HT) [42]. Yao et al. investigated the antibacterial properties of Cu nanoparticles containing TiO$_2$ coating synthesized by MAO [45]. Huang et al. fabricated the Cu-incorporated bioceramic coatings by MAO and HT and they evaluated osteoblast response [51]. Zhu et al. produced Cu-containing micro arc oxidized TiO$_2$ coatings and evaluated anti-bacterial properties [52]. Zhang et al. examined the antibacterial properties of TiO$_2$ coatings doped with various amounts with Cu nanoparticles deposited on titanium by MAO [53]. Huang et al. prepared Cu-containing TiO$_2$ coatings on Ti by MAO and then, biocompatibility and antibacterial properties were evaluated [54]. Zhang et al. directly fabricated Cu-doped TiO$_2$ coatings in alkaline electrolyte containing β-glycerophosphate disodium, calcium acetate and various amounts of copper acetate on Ti via a single step MAO process [55]. They then investigated in vitro biocompatibility and antibacterial activity for gram positive *S. aureus* [55]. However, in the above studies, Cu nanoparticles were randomly separated through the whole MAO surface. Also, for Cu-incorporated- and Cu containing-MAO coatings, Cu was not homogeneously distributed throughout the MAO surface. So, antibacterial adhesion properties on the Cu-MAO surface could not be sufficiently improved. Furthermore, Wu et al. produced Cu-doped TiO$_2$ coatings on cp-Ti by magnetron sputtering with MAO [56]. The CuTi layers were formed on the titanium substrate by magnetron sputtering at the first stage. Then, the bioceramic coatings were produced by MAO technique at the second stage. Afterwards, their antibacterial properties were evaluated [56]. However, in that study, the Cu was observed around micro discharge channels and could not be dispersed throughout the MAO surface. Moreover, in vitro bioactivity of the Cu-MAO

coatings were not investigated, although in vitro biocompatibility investigations were carried out in the above aforementioned studies.

In this work, unlike the literature, convenient two-step MAO and PVD-TE techniques were devoted to synthesis uniform, bioactive, biocompatible and anti-bacterial novel Cu-based TiO_2 bioceramic composite coatings on cp-Ti substrate. A bioactive and biocompatible anatase and rutile-based bioceramic structure on the cp-Ti substrate were coated by MAO technique in an alkaline electrolyte, consisting of Na_3PO_4 and KOH in de-ionized water at the first step. Then, a copper (Cu) nano-layer with 5 nm thickness was accumulated on the MAO coatings by the PVD-TE technique at the second step. The phase structures, morphologies, elemental amounts, functional groups, thicknesses, roughness and wettability of the MAO and Cu-based MAO coating surfaces were characterized by XRD (powder- and TF-XRD), SEM, EDS, FTIR, eddy current device, profilometer and CAG in detail, respectively. In vitro bioactivity of all coatings was evaluated by immersion tests in SBF at body temperature (36.5 °C) for 28 days. Then, for gram-positive bacteria (*Staphylococcus aureus*) and gram-negative bacteria (*Escherichia coli*), in vitro antibacterial properties of all coatings were investigated in detail.

2. Materials and Methods

2.1. Sample Preparation

The cp-Ti (Grade 2; commercially pure titanium) substrates were cut appropriate sizes (60 mm × 25 mm × 5 mm) by using a water jet. The surfaces of cp-Ti were ground by using silicon carbide (SiC) sand papers from No. 120 to No. 1200. And then, they were cleaned in an ultrasonic bath containing acetone for 60 min and dried in an oven at 50 °C.

2.2. Micro Arc Oxidation (MAO) Process

In order to produce bioceramic coatings on cp-Ti, an alternating current (AC) MAO device (MDO-100WS) running up to 100 kW was used. The MAO device mainly contained four pieces of equipment, consisting of an AC power supply, a double walled stainless steel tank, water cooled chiller and air flow stirrer. The cp-Ti was used as an anode, while the stainless-steel container was used as a cathode during MAO. The MAO solution was prepared by the dissociation of 10 g/L Na_3PO_4 and 1 g/L KOH in de-ionized water, respectively. The MAO treatment was performed on a constant current mode in the range of 0.325 A/cm^2 in Na_3PO_4 and KOH. The treating time was carried out at 5 min. The detailed MAO parameters and analysis results are given in Table 1. The temperature was maintained below 30 °C by a chiller in the tank during the MAO treatment. After the MAO treatment, all substrates were rinsed by de-ionized water and dried again in an oven at 50 °C for 24 h. Afterwards, they were preserved in desiccators. In order to ensure repeatability during MAO process, three MAO surfaces were produced on three cp-Ti specimens by the same parameters.

Table 1. The MAO coating parameters and the surface analysis results of the coatings such as thickness.

Electrolyte	Treatment Time (min)	Applied Power (μF)	The Sizes (mm^3)	Current Density (A/cm^2)	Average Thickness (μm)	Average Roughness (μm)
Na_3PO_4, KOH, Distilled water	5	150	60 × 25 × 5	0.325	60.0 ± 1.0	1.07

2.3. Physical Vapor Deposition-Thermal Evaporation (PVD-TE) Process

A Cu thin film layer with 5 nm (Copper: 99.999% purity of Alfa Aesar, Ward Hill, MA, USA) was accumulated on the MAO coatings using PVD-TE (Vaksis, Bilkent, Turkey, PVD/2T) at a deposition

speed of 0.5 nm/s at room temperature. The vacuum chamber pressure was set at about 1×10^{-6} mbar before the PVD-TE process started. The vacuum chamber pressure was maintained under vacuum (base pressure) of 3×10^{-5} mbar. In order to avoid the abrupt evaporation of Cu powders, the changeable current was gradually increased up to 45 A. The evaporated materials (Cu powders) with a grain size of -100 mesh were placed at the bottom of a wolfram crucible, that was approximately 15 cm away from the MAO coating surfaces. The average thickness of Cu nano-layer on the MAO surfaces was measured as about 5 nm by XTM integrated to PVD-TE device (Vaksis, Bilkent, Turkey, PVD/2T). Cu vapor products were then deposited onto the MAO surfaces. In order to ensure repeatability during the PVD-TE process, three Cu nano-layers were deposited on three MAO coating specimens by the same PVD-TE parameters.

2.4. Characterization of the Coatings

The phase structure of the MAO surfaces was detected by powder-XRD (powder-X-ray diffractometer, Bruker D8 Advance, Billerica, MA, USA) with Cu-Kα (λ = 1.54 Å) between 2θ values of 10° and 90° with a scanning rate of 0.1°·min^{-1}. The phase structure of Cu-based MAO coatings was analyzed by TF-XRD (Thin film-X-ray diffractometer, PANalytical X'Pert PRO MPD, Philips, Amsterdam, The Netherlands) with Cu-Kα between 2θ values of 10° and 90° with a scanning rate of 0.001°·min^{-1}. The surface morphologies of all coatings were analyzed by SEM (Scanning electron microscope, Philips XL30S FEG, Amsterdam, The Netherlands). Also, the elemental amounts of all coatings were evaluated by EDS (Energy dispersive spectrometer, Philips, Amsterdam, The Netherlands). The 3-D surface topography and surface roughness were evaluated by profilometer (surface profiler, KLA Tencor P-7, Milpitas, CA, USA). The surface roughness values were achieved by the scanning of mechanical contact at 500 μm $\times$ 500 μm area in 3-D. The surface wettability (hydrophilicy/hydrophobicity) and the contact angle values of all surfaces were analyzed by CAG (Contact Angle Goniometer, Dataphysics OCA 15EC, San Jose, CA, USA) sessile drop technique. The contact angle data was recorded throughout every 10 s from 0 to 90 s after the de-ionized water droplet of volume 1 μL was contacted onto the both surfaces.

2.5. In Vitro Bioactivity Tests

To be informed of in vitro apatite-forming ability on the MAO and Cu-based MAO surfaces, all coatings were immersed in 1.0$\times$ SBF (simulated body fluid) at body temperature (36.5 °C) for 28 days. The SBF procures the formation of bone-like apatite layer on the implant surfaces. So, the apatite-forming ability on the implant materials represents information predicted about in vitro bioactivity. The MAO and Cu-based MAO coating samples were immersed in 1.0$\times$ SBF with ion concentrations almost equal to that in human blood plasma. The SBF was prepared by dissolving reagent grade chemicals consisting of NaCl, NaHCO$_3$, KCl, K$_2$HPO$_4$·3H$_2$O, MgCl$_2$·6H$_2$O, CaCl$_2$ and Na$_2$SO$_4$ in distilled water at 36.5 °C, respectively. They were then buffered at pH 7.4 with (CH$_2$OH)$_3$CNH$_2$ and 1 M HCl at 36.5 °C. The surface area' ratio (in mm^2) of all surfaces to SBF was almost set 1 equal to 10 in the direction of the Kokubo and Takadama' recipe [57]. To maintain ion concentration of the SBF, it was renewed during every 24 h. All coating specimens were taken out from SBF at the post-immersion test and they were gently washed in de-ionized water. Eventually, they spontaneously dried under room temperature. All immersed dried coating specimens were kept in desiccators at pre-characterization. All experimental studies were carried out in triplicate.

After immersion treatment was completed in SBF, the morphologies, elemental structures, phase structures and functional groups of all coating surfaces were analyzed by SEM, EDS, TF-XRD and FTIR, respectively. The SEM images were taken with up to 20000$\times$ magnification. In addition, to reveal newly formed elements on immersed surfaces, all coatings surfaces were examined by EDS. The phase compositions of both coating surfaces were investigated by TF-XRD. The FTIR (Fourier transform infrared spectroscopy; JASCO FT/IR 6600, JASCO, Easton, MD, USA) spectra were collected over the range in the spectral range of 450–4000 cm^{-1} at post-immersion in SBF.

2.6. In Vitro Antibacterial Activity of the Coatings

The antibacterial activities of all coating surfaces were investigated versus to *S. aureus* and *E. coli* by colony counting method. All coating surfaces were immersed in 5.0 mL of the bacterial suspension (1×10^7 CFU/mL). They were then incubated at 37 °C for 24 h. All coatings samples were washed by 150 mM NaCl at post-incubation and put into a tube including 2 mL phosphate buffer solution. Subsequently, to detach the bacteria from the surfaces to solution, they were shaken on a vortex for 2 min. Aliquots of the solution with 100 µL were plated onto muller hinton agar (MHA) plates. The active bacteria colonies on the surfaces were then incubated at 37 °C for 48 h, and were counted. All experimental studies were carried out in triplicate.

3. Results and Discussion

3.1. Phase Structures of the Coatings

The phase structures of the MAO and Cu-based MAO coatings on cp-Ti were investigated by powder XRD and TF-XRD as shown in Figures 1 and 2, respectively. In addition to the cp-Ti substrate diffraction peaks (JCPDS card number: 044-1294), the existences of characteristic peaks of anatase-TiO_2 (JCPDS card number: 21-1272) and rutile-TiO_2 (JCPDS card number: 21-1276) on the MAO surface were indicated by the powder-XRD pattern as shown in Figure 1.
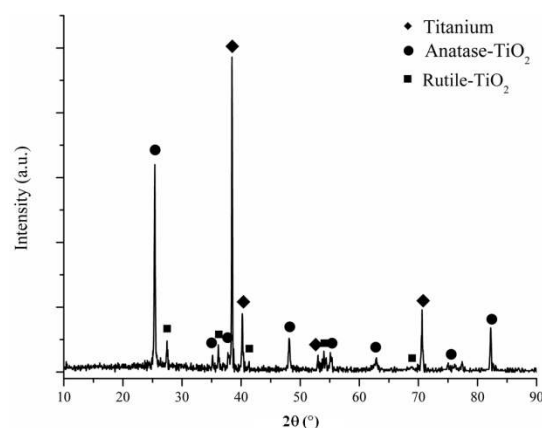

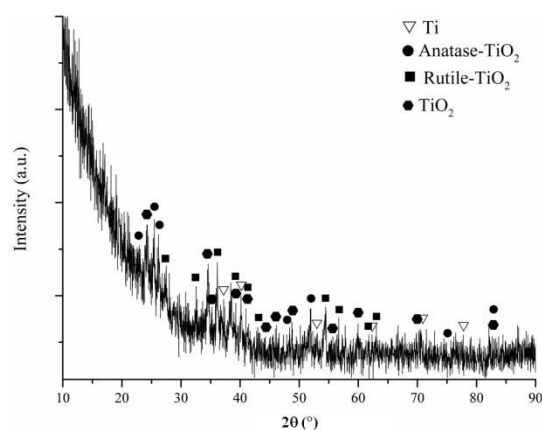**Figure 1.** XRD spectra pattern of the MAO coating.

Figure 2. TF-XRD spectra pattern of the Cu-based MAO coating.

After Cu was accumulated on the MAO surface, the phase structures formed on the surface were detected by TF-XRD as shown in Figure 2. The Ti (JCPDS card number: 04-004-8480), TiO_2 (JCPDS card number: 01-070-2556), anatase-TiO_2 (JCPDS card number: 01-083-5914) and rutile-TiO_2 (JCPDS

card number: 04-006-8034) were obtained on the Cu-based MAO surface as illustrated in Figure 1. The presence of crystalline Cu and/or Cu-based compounds were not verified by TF-XRD.

The phase of TiO_2 has two polymorphs, which are also known as anatase and rutile. The phase of rutile is stable at high temperatures, while the anatase is a metastable phase at low temperature. The phase of anatase forms, which is a metastable structure, on cp-Ti surface at initial steps of MAO process. It is reported that the amount of anatase in the coatings decreases, as the amount of rutile increases. It is clearly stated that the rutile modifier becomes predominant after a critical period of MAO parameters such as treatment time, voltage and current. So, the anatase transforms to thermodynamically stable rutile with increasing experimental parameters, such as treatment time, voltage and current at the next stages of the MAO process [9,58].

Anatase and rutile phases formed on the cp-Ti surface through the MAO process occurred by the ionization mechanism and electrostatic interactions of oppositely charged ions (anion and cation). The alkaline electrolyte consists of Na_3PO_4, and KOH compounds contain Na^+, $PO_4{}^{3-}$, K^+ and OH^- ions. The Na_3PO_4 is dissolved in distilled water and ionizes to Na^+ and $PO_4{}^{3-}$ (Equation (1)). Similarly, another compound of KOH is dissolved in de-ionized water and transforms to K^+ and OH^- ions (Equation (2)). Ti metals were dissolved and lost four electrons through MAO. Thereby, it transformed to positively charged cationic Ti^{4+} ions (Equation (3)). Synchronically, O_2 gaseous is released. The O_2 will either evolve as a gas, or dissolve into the solution as atoms and ionize to O^{2-}. Also, positively charged Ti^{4+} and negatively charged O^{2-} and/or OH^- ions react with each other due to the electrostatic interaction through MAO (Equations (4) and (5)). Eventually, the anodic oxidation reactions occur between cationic Ti^{4+} and anionic O^{2-}/OH^- ions on Ti substrate through the MAO. So, TiO_2 phase structure forms on cp-Ti substrate. The Gibbs energy of the anatase/rutile transition is negative because the phase of anatase is thermodynamically unstable for all temperature values. Anatase/rutile transition begins above 880 K and a completes at 1190 K [59]. The anatase to rutile transformation facilitates because the local temperature in micro discharge channels can reach 8000 K due to electron collisions through the MAO process [60]. Therefore, the amount of rutile increases with increasing MAO parameters such as treatment time, voltage and current.

Dissolution reactions in electrolyte:

$$Na_3PO_4 \rightarrow Na^+ + PO_4{}^{3-} \tag{1}$$

$$KOH \rightarrow K^+ + OH^- \tag{2}$$

$$Ti \rightarrow Ti^{4+} + 4e^- \tag{3}$$

Anodic oxidation reactions through MAO process:

$$Ti^{4+} + 4OH^- \rightarrow TiO_2 + 2H_2O \tag{4}$$

$$Ti^{4+} + 2O^{2-} \rightarrow TiO_2 \tag{5}$$
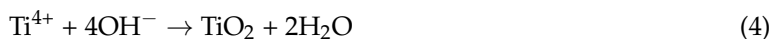
3.2. Surface Structures of the Coatings

The surface morphologies of the MAO and Cu-based MAO coatings on cp-Ti were evaluated by SEM as shown in Figure 3. As seen in Figure 3, the surfaces of both coatings are porous and rough. The MAO coatings contain many crater-like or volcano-like micro pores and a few micro cracks due to the existence of thermal stresses during whole process. The various-sized micro pores on the MAO surface are called as micro discharge channels occur by micro spark discharge. The micro sparks form at weak regions such as sites and edges on cp-Ti substrate during oxide film due to the existence of dielectric breakdown at the initial steps of the MAO process. Thus, these resulted in the increase of the intensity of micro discharge channels throughout the MAO process. The micro discharge channels

have various sizes and occur on the substrate materials though the MAO process. So, volcano-like structures are observed on the MAO surfaces. Molten oxide structures term as oxide magma occur in micro discharge channels owing to the existence of local high temperature (up to about 10^4 K) and high pressure (approximately 100 MPa) [61,62]. The molten oxides in micro discharge channels is rapidly cooled and solidified because it comes into contact with the electrolyte during MAO. Eventually, it stacked instantaneously to form the MAO coatings. These porous and rough surfaces are beneficial to cell attachment and lead to increased cell adhesion [63]. Moreover, it is reported that porous TiO_2 layers that promote the sinking of liquid into the pores owing to capillary forces are favorable for the seeding and spreading of cells [64,65].
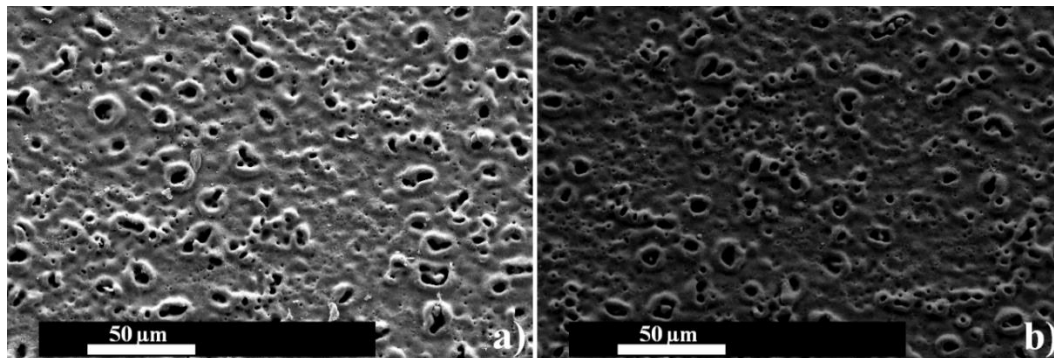

Figure 3. Surface SEM morphologies of the coatings: (**a**) the MAO coating and (**b**) Cu-based MAO coating.

The morphologies of both coating surfaces are nearly identical as shown in Figure 3, although TE treatment is applied on the MAO surface. The Cu layer has approximately 5 nm thickness and could not change the MAO surface or fill porous structure. In our previous studies [66,67], the hydroxyapatite-based MAO surface on zirconium was coated by anti-bacterial silver and zinc elements with 20 nm thickness and the surface morphology could not be changed. However, the surface chemistry, hydrophilicity/hydrophobicity, apatite forming ability and antibacterial activity are changed although morphologies of the MAO coating surfaces are maintained after the TE process. The 3-D mapping average roughness values of the MAO and Cu-based MAO surfaces are obtained as 1.10 and 1.16 µm, respectively. Thus, the average roughness of both surfaces was not significantly changed.

3.3. Elemental Chemical Analysis of the Coatings

The elemental analysis spectra results (the elemental amounts) on the MAO and Cu-based MAO coatings were analyzed by EDS and are shown in Table 2. A trace of Cu element was detected on the Cu-based surface while the elements of Ti, O and P were observed on both surfaces. The Ti peaks originate from the substrate material and TiO_2 structure in MAO coating. Furthermore, the O and P elements consist of anionic compounds such as PO_4^{3-} and OH^- in Na_3PO_4 and KOH-based alkaline MAO electrolyte. Anionic compounds migrate from electrolyte to substrate due to the existence of opposite charged ions under electrical field through MAO. Afterwards, they react with positively charged cationic ions (Ti^{4+}) accumulate on the MAO coating. However, the P element is not a crystalline form as seen in Figures 1 and 2 because it could not be detected by powder- or TF-XRD. The existence of the possible Ti-P-based compounds could not be proven in Figures 1 and 2. It can be expressed that they could not be transformed from amorphous to crystalline form on the surfaces whereas Ti^{4+} and PO_4^{3-} react with each other during MAO as supported by Figures 1 and 2. So, it could be stated that P-based compounds are an amorphous structure on the MAO-based surfaces. Moreover, the Cu was homogeneously stratified at a nanometer scale through the whole surface by TE process in that it is deposited on the MAO surface. The existence of the Cu element on the MAO surface is verified by the EDS-area whereas the crystallinity of it could not be confirmed by TF-XRD as shown in Figure 2.

Thus, it is observed as a trace amount on the MAO and TE combined surface. The Cu alters the surface chemistry of the MAO without any morphological changing as shown in Figure 3. Furthermore, it can be concluded that the Cu film on the MAO surface is an amorphous structure.

Table 2. EDS area spectra results of the MAO and the Cu-based MAO coatings.

Elements	The MAO Coating		The Cu-Based MAO Coating	
	wt.%	at.%	wt.%	at.%
O	34.82	60.03	33.06	58.23
P	7.76	6.91	8.53	7.76
Ti	57.42	33.06	55.94	32.91
Cu	–	–	2.48	1.10

3.4. Wettability of the Coatings

The wettability (hydrophilicity/hydrophobicity) of both surfaces was evaluated by a CAG device as shown in Table 3. Also, the average contact angle values of the coatings dependent on contacting time were given in Table 3 after the water droplet made contact with the surface. The CAG measurement is an efficient method to stay on top of the surface wettability and the surface free energy [68]. A small contact angle value refers to good wettability as a high contact angle value indicates a poor wettability. For orthopedic and dental implant applications, a good surface hydrophilicity is necessary for adherent growth of cell and tissue and it represents a good biocompatibility [68–71]. Furthermore, this was supported by in vitro apatite-forming ability results (in Section 3.5).

Table 3. The average contact angle values of the MAO and Cu-based MAO surfaces at post-contacting time of droplet.

The Droplet' Contacting Time (s)	The Contact Angle Values of the Substrates (°)	
	MAO Coating	Cu-Based MAO Coating
0	93.9	94.1
10	86.8	85.3
20	85.2	82.9
30	84.3	81.5
40	83.8	80.4
50	83.1	79.8
60	82.9	79.2
70	82.4	78.8
80	81.9	78.2
90	81.4	77.6

The surface wettability depends on many factors such as surface morphology, surface chemistry, roughness etc. [72,73]. The volcano-like pores on the surface absorb contacted distilled water by owing to capillary forces. So, for both surfaces, the contact angle values gradually decrease with increasing contact time as expected. Also, both surfaces exhibit hydrophilic characteristics because the contact angle values are lower than 90° [74]. It is clearly stated that TiO_2-based MAO surfaces are rough, indicating hydrophilic properties [75].

There is no extreme difference in contact angle values of both coatings, as shown in Table 3. However, it is obvious that the Cu-based surface is more hydrophilic than the MAO surface. In this study, the wettability of the surfaces change, whereas the surface morphologies of them are nearly identical. In a previous study [66], the surface of Zn-based with 5 nm thickness hydroxyapatite-based coating on zirconium was super hydrophilic with respect to the plain MAO surface. Similarly, another study [67], the surface of Ag-based with 20 nm thickness hydroxyapatite-based coating on zirconium was observed more hydrophobic than the one of plain MAO surface. So, it could be concluded that the hydrophilic/hydrophobic nature of the surfaces are strongly related to the surface chemistry even if the surfaces have identical morphology. Moreover, it is clear that the hydrophilicity of the MAO

surface is improved after the Cu with 5 nm thickness is deposited on the MAO surface. Essentially, these two different surfaces' wettability is related to the polarity of them. The polar surfaces indicate that hydrophilicity/lower contact angles improve the wettability, while the opposite trend is observed in non-polar surfaces [76]. Eventually, it could be concluded that the accumulation of Cu onto the MAO increases the wettability/hydrophilicity. Also, this situation is beneficial for the attachment of cell and tissue for medical applications.

3.5. In Vitro Bioactivity of the Coatings

It is claimed that newly formed bone-like apatite layers on its surface under living body conditions is an essential requirement for binding bone tissue of the implant materials. This situation refers to in vivo apatite formation on the implant materials. An apatite structure on the surface can occur by immersion in SBF up to week-long periods under body temperature (36.5/37 °C) except for in vivo experimental conditions. The apatite formation/apatite forming ability on the surface provides predictive information about in vitro bioactivity. Thus, in vitro apatite forming ability on the surface is an important assessment to evaluate the bioactivity of the implants. However, "Apatite-forming ability is just a necessary but by no means sufficient precondition of "bioactivity". "Bioactivity" is a very complex interplay of many factors, where apatite-forming ability is just one of many" [77]. So, in order to be predicting information about bioactivity of all coating surfaces, in vitro immersion test was carried out under SBF condition at 36.5 °C for 28 days. After immersion tests were completed, the morphologies, elemental amount, phase structure and functional groups of all surfaces were characterized by SEM, EDS-area, TF-XRD and FTIR, respectively as seen in Figure 4, Table 4, Figures 5 and 6.
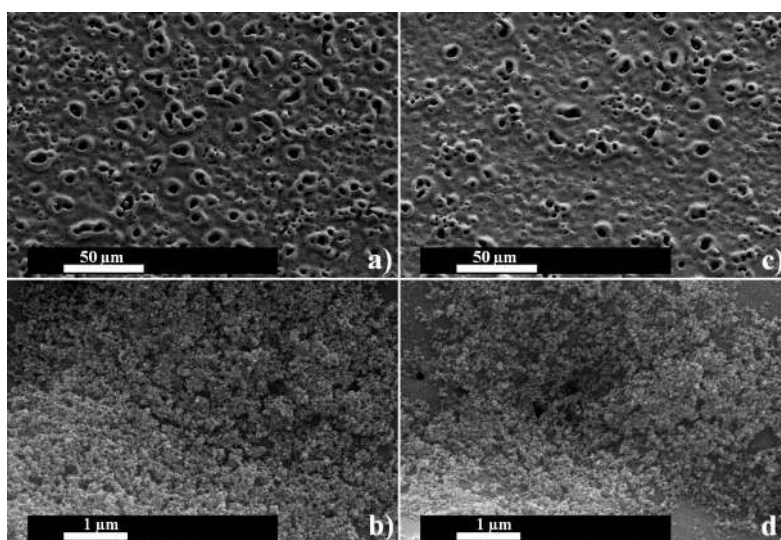

Figure 4. Surface morphologies of the coatings at post-immersion in SBF at 36.5 °C for 28 days: (**a**) 500× and (**b**) 20000× for the MAO surface and (**c**) 500× and (**d**) 20000× for the Cu-based MAO surface.

Table 4. EDS area spectra results of the MAO and the Cu-based MAO coatings at post-immersion in SBF.

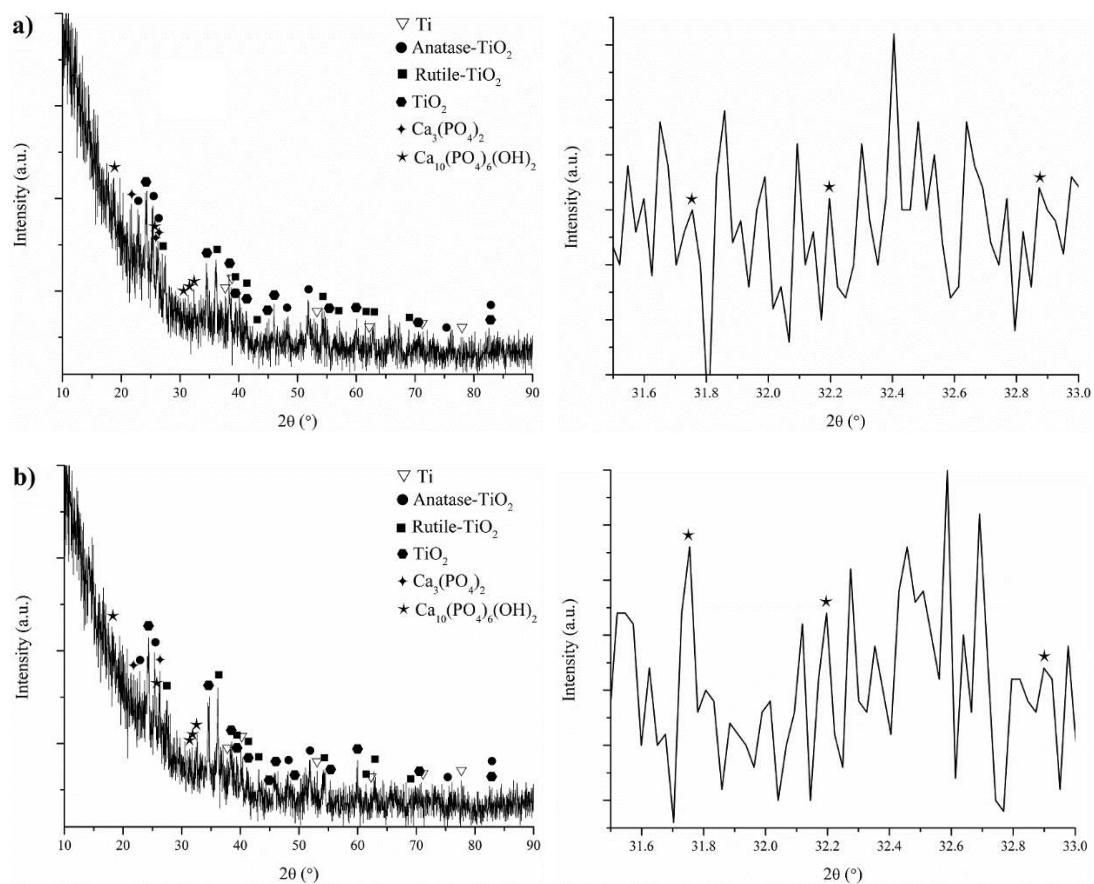| Elements	The MAO Coating		The Cu-Based MAO Coating	
	wt.%	at.%	wt.%	at.%
O	43.82	68.48	37.88	63.15
P	7.28	5.88	7.27	6.26
Ca	1.27	0.79	0.85	0.56
Ti	47.63	24.86	53.73	29.91
Cu	–	–	0.27	0.11

Figure 5. TF-XRD spectra pattern of the coatings at post-immersion in SBF at 36.5 °C for 28 days: (**a**) the MAO coating and (**b**) Cu-based MAO coating.
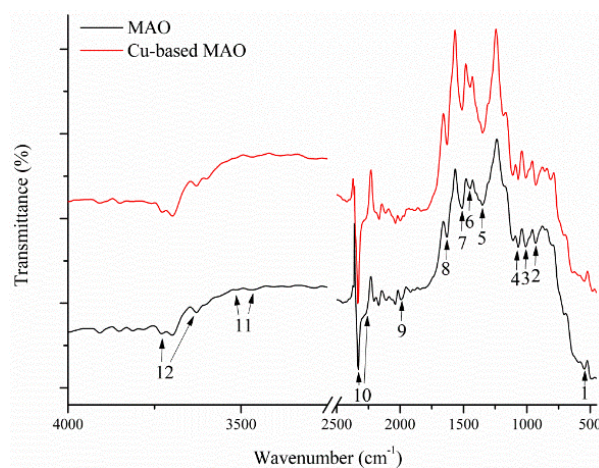

Figure 6. FTIR spectra of the coatings at post-immersion in SBF at 36.5 °C for 28 days: (black line) the MAO coating and (red line) Cu-based MAO coating.

After immersion in SBF for 28 days, the morphologies of both coating surfaces were investigated by SEM as shown in Figure 4. It could be clearly observed that the fine-dispersed particles are well dispersed throughout the whole surface at the post-immersion process. These fine-dispersed particles are nearly coated on the surfaces as seen in Figure 4. These particles are well dispersed through the whole surface. However, it is observed that the dispersed particles formed on the Cu-based surface are a little thinner than the one on the MAO surface at micron scales. It is well known that the crystalline apatite structure formed on the surfaces refers to predicting bioactivity. Therefore, as seen in TF-XRD

and FTIR spectra results, the existence of crystalline apatite structure on the Cu-based MAO surface are greater than one the MAO surface whereas the apatite layer on the Cu-based MAO surface is a little thin respect to the MAO surface at macron scales scanning ($10^6 \times 10^6$ μm^2). So, it can be stated that the Cu-nano layer on the MAO surface triggers increasing the crystallinity of apatite structure under SBF.

In order to get information, the elemental structures and the elemental amounts of both surfaces at post-immersion in SBF, the MAO and Cu-based MAO surfaces were analyzed by the EDS-area as shown in Table 4. In addition to the existence of Ti, O, P and Cu detected on the surfaces at pre-immersion in SBF as given in Table 2, an extra Ca element is obtained on both surfaces at post-immersion in SBF as given in Figure 5 and Table 4. The presence of this is connected with the diffusion Ca^{2+} ions of Ca-based SBF surfaces onto the surfaces during the immersion process. Positively charged Ca^{2+} ions in SBF migrate on the Ti-OH based surfaces due to the electrostatic interactions of oppositely charged ions. Then, PO_4^{3-} and OH^- ions in SBF diffuse to both surfaces. These migrations and reactions are carried out through the immersion process in SBF. Eventually, they formed an apatite layer on the surfaces during the post-immersion process. Thus, an extra Ca element is observed on both surfaces during the post-immersion process. However, the electron penetration depth varies from 0.2 to 2 μm, depending on the accelerating voltage in EDS analysis. Thus, only presented elements in these particles formed at the post-immersion process in SBF cannot be observed by EDS. Besides the elements in these particles, the elements such as Ti, O, P and Cu existed in the MAO and PVD layer were observed by EDS analysis.

The phase structures of these newly formed dispersed structures were characterized by TF-XRD and FTIR as shown in Figures 5 and 6. The phases of Ti (JCPDS card number: 04-004-8480), anatase (JCPDS card number: 01-083-5914), rutile (JCPDS card number: 04-006-8034), TiO_2 (JCPDS card number: 01-070-2556), TCP (tri-calcium phosphate: (JCPDS card number: 044-1294)) and apatite (JCPDS card number: 00-009-0432) on the MAO and Cu-based MAO surfaces at post-immersion in SBF were observed in Figure 5a,b, respectively. The existences of Ti, TiO_2, anatase and rutile on both surfaces have been verified in Figures 1 and 2 at pre-immersion in SBF. The phases of TCP and apatite on both surfaces form at post-immersion in SBF under body temperature for 28 days. So, the fine-dispersed particles monitored in Figure 4 refer to TCP and apatite phases on immersed surfaces. As seen in Figure 5a,b, the intensity and amount of crystalline apatite structure on the Cu-based MAO are greater than ones on the MAO whereas the elemental amounts of Ca on the Cu-based MAO are lower than one on the MAO as reported in EDS-area spectra and amount results. The apatite-forming ability on the Cu-based MAO surface is high compared to the MAO surface according to TF-XRD spectra.

The functional groups and phases on the MAO and Cu-based MAO coatings at post-immersion in SBF were investigated by FTIR as seen in Figure 6. Also, at post-immersion in SBF, FTIR spectrum analysis results such as wave numbers, band modes, band assignments and phase were presented in Table 5. The band structures obtained on both surfaces at post-immersion in SBF are (PO_4^{3-}), (C–C), (CO_3^{2-}), (OH^-), (P–H) and (Ti–O–Ti). The FTIR spectra curves found at 560 and 1026, 962 and 1050, 1403, 1420–1425 and 1460–1465, 1641, 1980 and 2302–2388, 3397–3448 and 3640–3742 cm^{-1} correspond to (PO_4^{3-}), (PO_4^{3-}), (C–C$^-$), (CO_3^{2-}), (OH^-), (P–H), (Ti–O–Ti) and (OH^-), respectively [22,43,78–95]. The ATR-FTIR peaks of both surfaces verify the presence of (C–C) at 1403 cm^{-1} [43,78–80], the presence of (OH^-) ion at 1641 cm^{-1} [43,78,79] and the presence of (Ti–O–Ti) in the regions of 3397–3448 cm^{-1} [43,78–80]. In addition to XRD spectra, the presence of TiO_2 structure on both surfaces are indicated by the bands of (C–C), (OH^-) and (Ti–O–Ti) on FTIR once again [43,78–80]. The FTIR spectra curves on both surfaces refer to the presence of (PO_4^{3-}) at 560 cm^{-1} [81–83] and 1026 cm^{-1} [83–86], the presence of (PO_4^{3-}) at 962 cm^{-1} [83–87] and 1050 cm^{-1} [83–87], the presence of (P–H) in the regions of 1980 cm^{-1} [88–93] and 2302–2388 cm^{-1} [88–93] and the presence of (OH^-) at 3640–3742 cm^{-1} [88,91–94]. The apatite and TCP structures formed on both surfaces at post-immersion in SBF are proved by the presence of (PO_4^{3-}), (P–H) and (OH^-) bands on FTIR curves [81–94]. The FTIR spectra curves on both surfaces verify the presence of (CO_3^{2-}) at 1420–1425 cm^{-1} [22,95] and 1460–1465 cm^{-1} [22,95]. The substituted carbonated-apatite formed on both surfaces at post-immersion

in SBF is proved by the presence of (CO_3^{2-}) [22,95]. It is clear that the induced apatite is a carbonated apatite at post-immersion in SBF for 28 days. It is well known that the sharp and deep of FTIR peaks provide information about the crystallinity of phases on the surface [96]. As supported in Figure 5, the sharp and deep peaks of (PO_4^{3-}) bands in the Cu-based MAO verify the existence of highly crystalline apatite structure respect to the MAO in Figure 6. Thus, it can be stated that the Cu on the MAO improve predicting bioactivity compared to the MAO surface.

Table 5. ATR-FTIR spectrum analysis results for the MAO and Cu-based MAO coatings after immersion in SBF.

Peak Number	Wavenumber (cm^{-1})	Band Assignment	Band Mode	Phase Structures	References
1	560	PO_4^{3-}	Stretching	Apatite	[81–83]
2	962	PO_4^{3-}	Stretching	Apatite, TCP	[83–87]
3	1026	PO_4^{3-}	Stretching	Apatite	[83–86]
4	1050	PO_4^{3-}	Stretching	Apatite, TCP	[83–87]
5	1403	C–C	Stretching	TiO_2	[43,78–80]
6	1420–1425	CO_3^{2-}	Stretching	A-type apatite	[22,95]
7	1460–1465	CO_3^{2-}	Stretching	B-type apatite	[22,95]
8	1641	OH^-	Stretching	TiO_2	[43,78,79]
9	1980	P–H	Stretching	Apatite	[88–93]
10	2302–2388	P–H	Stretching	Apatite	[88–93]
11	3397–3448	Ti–O–Ti	Stretching	TiO_2	[43,78–80]
12	3640–3742	OH^-	Stretching	Apatite	[88,91–94]

SBF is a metastable calcium phosphate-based electrolyte supersaturated compared to the apatite structure [97]. However, it is stated that a chemical stimulus is required to trigger the heterogeneous nucleation of apatite from the SBF because the homogeneous nucleation threshold of apatite is very high [98]. The hydroxyl groups such as Ti–OH on the surfaces are basically essential to induce the apatite nucleation. The provision of abundant Ti–OH groups and the enrichment of calcium and phosphate trigger the nucleation of apatite on the MAO surface [97]. After apatite nuclei forms on the surface, the ions of Ca^{2+}, PO_4^{3-} and CO_3^{2-} in SBF diffuse to TiO_2-based surfaces to combine with apatite nuclei owing to the electrostatic interactions of opposite charged ions. As a result, a novel apatite layer is formed on both coating surfaces.

3.6. In Vitro Antibacterial Activity of the Coatings

In order to determine the antibacterial contribution of the Cu layer on the MAO process, the level of bacterial colony adhering to the cp-Ti, the MAO (TiO_2) and Cu-based MAO surfaces was investigated. Figure 7 shows active colony ratios of gram-positive (*S. aureus*) and gram-negative (*E. coli*) bacteria adhered to all tested surfaces. Also, Figures 8 and 9 show *S. aureus* and *E. coli* colony plates formed by bacteria adhering to all surfaces after incubation, respectively. It was determined that the adhesion of gram-positive and gram-negative bacteria on the cp-Ti surfaces was lower than that of the MAO surface. The MAO surfaces containing bioactive and biocompatible TiO_2 structures are porous and rough. Thus, the surface energy of the MAO is greater than one of the smooth surfaces. Hence, it can be concluded that the active colony ratios of *S. aureus* and *E. coli* adhered on the MAO surfaces increased in very small amount compared to the smooth cp-Ti surfaces. However, this difference was not statistically significant ($p > 0.05$). So, the numbers of bacteria adhering to cp-Ti and the MAO surfaces were very close to each other.

The antibacterial activity of the Cu-based MAO surfaces against *E. coli* was determined as 68.0%. Also, the antibacterial activity of the Cu-based MAO surfaces against *S. aureus* was observed as 69.6%, respectively. It has been observed that Cu-based MAO coating process provides antibacterial property to the substrate and MAO surfaces. Also, the Cu coating increases the antibacterial property by 1.11-1.18-fold against *S. aureus* and *E. coli*, respectively. This result shows that the Cu-based MAO

coating on the surface has a significant effect on antibacterial activity. The increase in antibacterial activity by increasing the coating can be explained by the more intense interaction of Cu ions on the surface and bacteria.
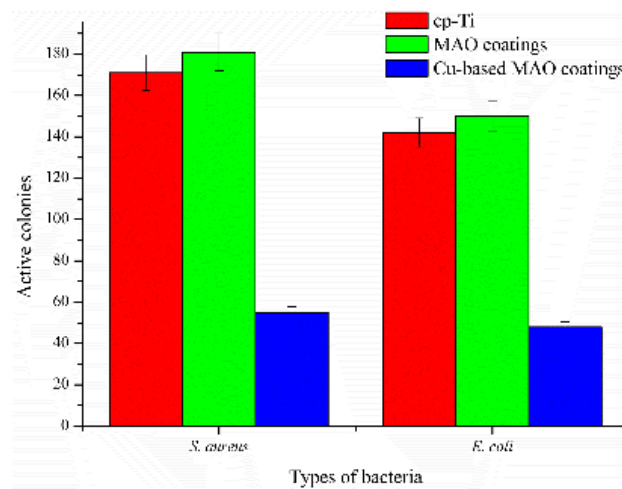

Figure 7. Active colony ratios of *S. aureus* as gram positive bacteria and *E. coli* as gram negative bacteria on cp-Ti substrate, the MAO and Cu-based MAO surface cultivation.
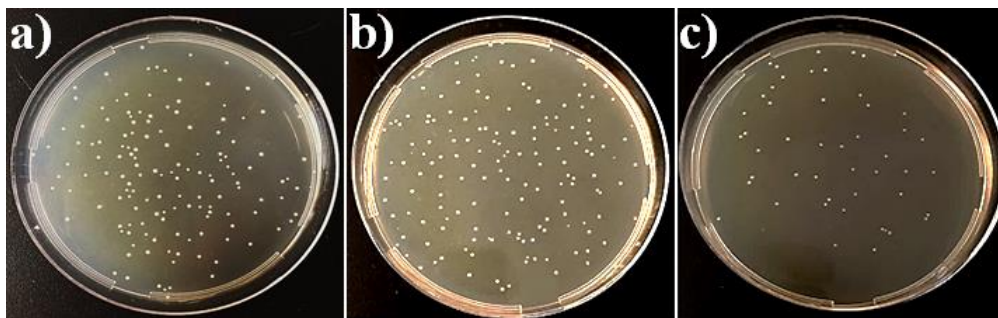

Figure 8. Culture plate photographs of *S. aureus* after re-cultivation: (**a**) cp-Ti substrate, (**b**) the MAO and (**c**) Cu-based MAO surface cultivation.
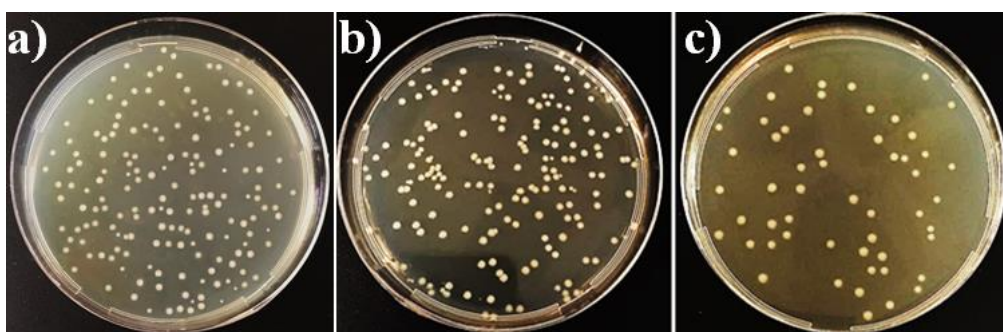

Figure 9. Culture plate photographs of *E. coli* after re-cultivation: (**a**) cp-Ti substrate, (**b**) the MAO and (**c**) Cu-based MAO surface cultivation.

The increase in antibacterial activity of surfaces after Cu-based coating may be explained by the toxic effect of Cu ions on the bacterial cell. In mediums containing Cu-based surfaces, bacteria are immobilized to the coated surfaces; proliferation and movement are restricted, and cell death occurs [99]. Copper causes toxic effects on the bacteria by multiple mechanisms and prevents the resistance formation in the bacteria. The first mechanism is that copper ions deform the cell wall and cause cell death. In another mechanism, copper ions inactivate membrane

proteins and enzymes, disrupt transporter molecules and lead to cell death [100,101]. Previously, some researchers have investigated the antibacterial properties of Cu-based MAO surfaces against various microorganisms [102,103]. Trapalis et al. [104] reported that copper-coated surfaces (Cu/SiO$_2$) exhibited significant antibacterial activity against *E. coli*.

Another important observation in this study is that Cu-based surfaces show higher antibacterial activity against *S. aureus* than *E. coli*. The Cu-based surfaces, which exhibit the highest antibacterial activity in this study, showed 1.02 times higher antibacterial activity against *S. aureus* compared to *E. coli*. This result can be explained by the structural differences of gram-positive and gram-negative cells. Gram-negative bacteria have an outer membrane in addition to the cell wall, while gram-positive bacteria do not have an outer membrane. The outer membrane acts as a barrier to reduce the transport of metals to the bacteria. For this reason, copper penetrates rapidly into the cell in gram-positive cells and a serious toxic effect occurs. However, in gram-negative bacteria containing outer membrane, copper transport to the cell is restricted; the formation of toxic effect is delayed and reduced [50,105]. Similar studies in the literature support these results. Wang et al. [105] reported that selenium-coated surfaces are more effective against gram-positive bacteria and that this result is due to the cellular difference between *S. aureus* and *E. coli*.

4. Conclusions

A novel Cu-based TiO$_2$ coating has been produced on cp-Ti surfaces by using combined two-step MAO and PVD-TE methods for dental implant applications. The TF-XRD spectra results showed that the existence of crystalline Cu on the MAO surfaces could not be observed whereas it was detected as elemental structure by EDS attached to SEM. Also, the SEM analyses indicated that the surface morphologies of the MAO and Cu-based MAO coatings were porous and rough. The morphology and topography of both coating surfaces were not changed by PVD-TE treatment. However, the hydrophilicity of Cu-based MAO surfaces was improved with respect to the MAO surfaces owing to the enhancing polarity of Cu on the MAO surface. Moreover, in vitro bioactivity of Cu-based TiO$_2$ surfaces was increased compared to the MAO surfaces after immersion test in SBF for 28 days. These were supported by TF-XRD, ATR-FTIR and SEM as written in Section 3.5. Furthermore, it was observed that the amounts of active-bacteria colonies lived on Cu-based MAO surfaces were lower than ones of the MAO surface for gram positive (*S. aureus*) and gram negative (*E. coli*).

There have been some remarkable studies on the production of antibacterial Cu/CuO-nanoparticles containing Cu-incorporated- and Cu-containing-TiO$_2$ coatings on Ti by a single or hybrid MAO methods [42,45,51–56]. However, Cu nanoparticles were randomly separated through the whole MAO surface in aforementioned studies. Also, Cu was not uniformly separated on Cu-incorporated- and Cu-containing-MAO surfaces. So, antibacterial adhesion properties on the Cu-MAO surface could not be sufficiently improved. Moreover, the Cu was observed around micro discharge channels and could not be dispersed during combined hybrid MAO surfaces. Moreover, in vitro bioactivity of the Cu-nanoparticles, Cu-incorporated and Cu-containing-MAO coatings were not investigated although in vitro biocompatibility investigations were carried out in aforementioned studies. In conclusion, it can be stated that the Cu-based TiO$_2$ coatings are porous, rough and have the potential for biomedical surface coating applications due to their hopeful properties such as surface chemistry, morphology, hydrophilicity, in vitro bioactivity and in vitro antibacterial resistance with respect to other literature studies.

Conflicts of Interest: The author declares no conflict of interest.

References

1.　Quintero, D.; Galvis, O.; Calderón, J.A.; Castaño, J.G.; Echeverría, F. Effect of electrochemical parameters on the formation of anodic films on commercially pure titanium by plasma electrolytic oxidation. *Surf. Coat. Technol.* **2014**, *258*, 1223–1231. [CrossRef]

2.　Yang, W.; Xu, D.; Guo, Q.; Chen, T.; Chen, J. Influence of electrolyte composition on microstructure and properties of coatings formed on pure Ti substrate by micro arc oxidation. *Surf. Coat. Technol.* **2018**, *349*, 522–528. [CrossRef]

3.　Teker, D.; Muhaffel, F.; Menekse, M.; Karaguler, N.G.; Baydogan, M.; Cimenoglu, H. Characteristics of multi-layer coating formed on commercially pure titanium for biomedical applications. *Mater. Sci. Eng. C* **2015**, *48*, 579–585. [CrossRef] [PubMed]

4.　Liu, J.-X.; Yang, D.-Z.; Shi, F.; Cai, Y.-J. Sol–gel deposited TiO_2 film on NiTi surgical alloy for biocompatibility improvement. *Thin Solid Films* **2003**, *429*, 225–230. [CrossRef]

5.　Duarte, L.T.; Bolfarini, C.; Biaggio, S.R.; Rocha-Filho, R.C.; Nascente, P.A.P. Growth of aluminum-free porous oxide layers on titanium and its alloys Ti-6Al-4V and Ti-6Al-7Nb by micro-arc oxidation. *Mater. Sci. Eng. C* **2014**, *41*, 343–348. [CrossRef] [PubMed]

6.　Terleeva, O.P.; Sharkeev, Y.P.; Slonova, A.I.; Mironov, I.V.; Legostaeva, E.V.; Khlusov, I.A.; Matykina, E.; Skeldon, P.; Thompson, G.E. Effect of microplasma modes and electrolyte composition on micro-arc oxidation coatings on titanium for medical applications. *Surf. Coat. Technol.* **2010**, *205*, 1723–1729. [CrossRef]

7.　Yoon, I.-K.; Hwang, J.-Y.; Jang, W.-C.; Kim, H.-W.; Shin, U.S. Natural bone-like biomimetic surface modification of titanium. *Appl. Surf. Sci.* **2014**, *301*, 401–409. [CrossRef]

8.　Albrektsson, T.; Jacobsson, M. Bone-metal interface in osseointegration. *J. Prosthet. Dent.* **1987**, *57*, 597–607. [CrossRef]

9.　Venkateswarlu, K.; Rameshbabu, N.; Sreekanth, D.; Bose, A.C.; Muthupandi, V.; Subramanian, S. Fabrication and characterization of micro-arc oxidized fluoride containing titania films on cp Ti. *Ceram. Int.* **2013**, *39*, 801–812. [CrossRef]

10.　Durdu, S.; Usta, M.; Berkem, A.S. Bioactive coatings on Ti6Al4V alloy formed by plasma electrolytic oxidation. *Surf. Coat. Technol.* **2016**, *301*, 85–93. [CrossRef]

11.　Drnovšek, N.; Rade, K.; Milačič, R.; Štrancar, J.; Novak, S. The properties of bioactive TiO_2 coatings on Ti-based implants. *Surf. Coat. Technol.* **2012**, *209*, 177–183. [CrossRef]

12.　He, X.; Zhang, G.; Wang, X.; Hang, R.; Huang, X.; Qin, L.; Tang, B.; Zhang, X. Biocompatibility, corrosion resistance and antibacterial activity of TiO_2/CuO coating on titanium. *Ceram. Int.* **2017**, *43*, 16185–16195. [CrossRef]

13.　Çomaklı, O.; Yazıcı, M.; Kovacı, H.; Yetim, T.; Yetim, A.F.; Çelik, A. Tribological and electrochemical properties of TiO_2 films produced on cp-Ti by sol-gel and silar in bio-simulated environment. *Surf. Coat. Technol.* **2018**, *352*, 513–521. [CrossRef]

14.　Uhm, S.-H.; Song, D.-H.; Kwon, J.-S.; Im, S.-Y.; Han, J.-G.; Kim, K.-N. Time-dependent growth of TiO_2 nanotubes from a magnetron sputtered Ti thin film. *Thin Solid Films* **2013**, *547*, 181–187. [CrossRef]

15.　Garcia-Valenzuela, A.; Alvarez, R.; Rico, V.; Cotrino, J.; Gonzalez-Elipe, A.R.; Palmero, A. Growth of nanocolumnar porous TiO_2 thin films by magnetron sputtering using particle collimators. *Surf. Coat. Technol.* **2018**, *343*, 172–177. [CrossRef]

16.　Cabanas-Polo, S.; Boccaccini, A.R. Electrophoretic deposition of nanoscale TiO_2: Technology and applications. *J. Eur. Ceram. Soc.* **2016**, *36*, 265–283. [CrossRef]

17.　An, S.-H.; Matsumoto, T.; Miyajima, H.; Sasaki, J.-I.; Narayanan, R.; Kim, K.-H. Surface characterization of alkali- and heat-treated Ti with or without prior acid etching. *Appl. Surf. Sci.* **2012**, *258*, 4377–4382. [CrossRef]

18.　Kim, S.-Y.; Kim, Y.-K.; Jang, Y.-S.; Park, I.-S.; Lee, S.-J.; Jeon, J.-G.; Lee, M.-H. Bioactive effect of alkali-heat treated TiO_2 nanotubes by water or acid treatment. *Surf. Coat. Technol.* **2016**, *303*, 256–267. [CrossRef]

19.　Weng, F.; Chen, C.; Yu, H. Research status of laser cladding on titanium and its alloys: A review. *Mater. Des.* **2014**, *58*, 412–425. [CrossRef]

20.　Sharifi, N.; Pugh, M.; Moreau, C.; Dolatabadi, A. Developing hydrophobic and superhydrophobic TiO_2 coatings by plasma spraying. *Surf. Coat. Technol.* **2016**, *289*, 29–36. [CrossRef]

21. Wang, H.-D.; He, P.-F.; Ma, G.-Z.; Xu, B.-S.; Xing, Z.-G.; Chen, S.-Y.; Liu, Z.; Wang, Y.-W. Tribological behavior of plasma sprayed carbon nanotubes reinforced TiO$_2$ coatings. *J. Eur. Ceram. Soc.* **2018**, *38*, 3660–3672. [CrossRef]

22. Zhou, R.; Wei, D.; Cheng, S.; Li, B.; Wang, Y.; Jia, D.; Zhou, Y.; Guo, H. The structure and in vitro apatite formation ability of porous titanium covered bioactive microarc oxidized TiO$_2$-based coatings containing Si, Na and Ca. *Ceram. Int.* **2014**, *40*, 501–509. [CrossRef]

23. Durdu, S.; Usta, M. The tribological properties of bioceramic coatings produced on Ti6Al4V alloy by plasma electrolytic oxidation. *Ceram. Int.* **2014**, *40*, 3627–3635. [CrossRef]

24. Du, Q.; Wei, D.; Wang, Y.; Cheng, S.; Liu, S.; Zhou, Y.; Jia, D. The effect of applied voltages on the structure, apatite-inducing ability and antibacterial ability of micro arc oxidation coating formed on titanium surface. *Bioact. Mater.* **2018**, *3*, 426–433. [CrossRef] [PubMed]

25. He, Y.; Zhang, Y.; Shen, X.; Tao, B.; Liu, J.; Yuan, Z.; Cai, K. The fabrication and in vitro properties of antibacterial polydopamine-ll-37-POPC coatings on micro-arc oxidized titanium. *Colloids Surf. B Biointerfaces* **2018**, *170*, 54–63. [CrossRef] [PubMed]

26. Sun, L.; Berndt, C.C.; Gross, K.A.; Kucuk, A. Material fundamentals and clinical performance of plasma-sprayed hydroxyapatite coatings: A review. *J. Biomed. Mater. Res.* **2001**, *58*, 570–592. [CrossRef] [PubMed]

27. Manso, M.; Jiménez, C.; Morant, C.; Herrero, P.; Martínez-Duart, J.M. Electrodeposition of hydroxyapatite coatings in basic conditions. *Biomaterials* **2000**, *21*, 1755–1761. [CrossRef]

28. Lee, J.-H.; Kim, H.-E.; Shin, K.-H.; Koh, Y.-H. Electrodeposition of biodegradable sol-gel derived silica onto nanoporous TiO$_2$ surface formed on Ti substrate. *Mater. Lett.* **2011**, *65*, 1519–1521. [CrossRef]

29. Xu, L.; Wu, C.; Lei, X.; Zhang, K.; Liu, C.; Ding, J.; Shi, X. Effect of oxidation time on cytocompatibility of ultrafine-grained pure Ti in micro-arc oxidation treatment. *Surf. Coat. Technol.* **2018**, *342*, 12–22. [CrossRef]

30. Yilmaz, M.S.; Sahin, O. Applying high voltage cathodic pulse with various pulse durations on aluminium via micro-arc oxidation (MAO). *Surf. Coat. Technol.* **2018**, *347*, 278–285. [CrossRef]

31. Yang, W.; Xu, D.; Yao, X.; Wang, J.; Chen, J. Stable preparation and characterization of yellow micro arc oxidation coating on magnesium alloy. *J. Alloy. Compd.* **2018**, *745*, 609–616. [CrossRef]

32. Yang, W.; Xu, D.; Wang, J.; Yao, X.; Chen, J. Microstructure and corrosion resistance of micro arc oxidation plus electrostatic powder spraying composite coating on magnesium alloy. *Corros. Sci.* **2018**, *136*, 174–179. [CrossRef]

33. Zhang, D.; Ge, Y.; Liu, G.; Gao, F.; Li, P. Investigation of tribological properties of micro-arc oxidation ceramic coating on Mg alloy under dry sliding condition. *Ceram. Int.* **2018**, *44*, 16164–16172. [CrossRef]

34. Zhang, J.; Fan, Y.; Zhao, X.; Ma, R.; Du, A.; Cao, X. Influence of duty cycle on the growth behavior and wear resistance of micro-arc oxidation coatings on hot dip aluminized cast iron. *Surf. Coat. Technol.* **2018**, *337*, 141–149. [CrossRef]

35. Cui, L.-Y.; Liu, H.-P.; Zhang, W.-L.; Han, Z.-Z.; Deng, M.-X.; Zeng, R.-C.; Li, S.-Q.; Wang, Z.-L. Corrosion resistance of a superhydrophobic micro-arc oxidation coating on Mg-4Li-1Ca alloy. *J. Mater. Sci. Technol.* **2017**, *33*, 1263–1271. [CrossRef]

36. Fan, X.; Feng, B.; Di, Y.; Lu, X.; Duan, K.; Wang, J.; Weng, J. Preparation of bioactive TiO film on porous titanium by micro-arc oxidation. *Appl. Surf. Sci.* **2012**, *258*, 7584–7588. [CrossRef]

37. Zhang, C.L.; Zhang, F.; Song, L.; Zeng, R.C.; Li, S.Q.; Han, E.H. Corrosion resistance of a superhydrophobic surface on micro-arc oxidation coated Mg-Li-Ca alloy. *J. Alloy. Compd.* **2017**, *728*, 815–826. [CrossRef]

38. Wang, Y.; Yu, H.; Chen, C.; Zhao, Z. Review of the biocompatibility of micro-arc oxidation coated titanium alloys. *Mater. Des.* **2015**, *85*, 640–652. [CrossRef]

39. Wang, L.; Shi, L.; Chen, J.; Shi, Z.; Ren, L.; Wang, Y. Biocompatibility of Si-incorporated TiO$_2$ film prepared by micro-arc oxidation. *Mater. Lett.* **2014**, *116*, 35–38. [CrossRef]

40. Li, Y.; Wang, W.; Liu, H.; Lei, J.; Zhang, J.; Zhou, H.; Qi, M. Formation and in vitro/in vivo performance of "cortex-like" micro/nano-structured TiO$_2$ coatings on titanium by micro-arc oxidation. *Mater. Sci. Eng. C* **2018**, *87*, 90–103. [CrossRef]

41. Liu, X.Y.; Chu, P.K.; Ding, C.X. Surface modification of titanium, titanium alloys, and related materials for biomedical applications. *Mater. Sci. Eng. R-Rep.* **2004**, *47*, 49–121. [CrossRef]

42. Wu, Q.J.; Li, J.H.; Zhang, W.J.; Qian, H.X.; She, W.J.; Pan, H.Y.; Wen, J.; Zhang, X.L.; Liu, X.Y.; Jiang, X.Q. Antibacterial property, angiogenic and osteogenic activity of Cu-incorporated TiO$_2$ coating. *J. Mater. Chem. B* **2014**, *2*, 6738–6748. [CrossRef]

43. Durdu, S.; Aktug, S.L.; Korkmaz, K.; Yalcin, E.; Aktas, S. Fabrication, characterization and in vitro properties of silver-incorporated TiO$_2$ coatings on titanium by thermal evaporation and micro-arc oxidation. *Surf. Coat. Technol.* **2018**, *352*, 600–608. [CrossRef]

44. Hu, H.; Zhang, W.; Qiao, Y.; Jiang, X.; Liu, X.; Ding, C. Antibacterial activity and increased bone marrow stem cell functions of Zn-incorporated TiO$_2$ coatings on titanium. *Acta Biomater.* **2012**, *8*, 904–915. [CrossRef] [PubMed]

45. Yao, X.; Zhang, X.; Wu, H.; Tian, L.; Ma, Y.; Tang, B. Microstructure and antibacterial properties of Cu-doped TiO$_2$ coating on titanium by micro-arc oxidation. *Appl. Surf. Sci.* **2014**, *292*, 944–947. [CrossRef]

46. Wu, C.; Zhou, Y.; Xu, M.; Han, P.; Chen, L.; Chang, J.; Xiao, Y. Copper-containing mesoporous bioactive glass scaffolds with multifunctional properties of angiogenesis capacity, osteostimulation and antibacterial activity. *Biomaterials* **2013**, *34*, 422–433. [CrossRef] [PubMed]

47. Li, J.; Zhai, D.; Lv, F.; Yu, Q.; Ma, H.; Yin, J.; Yi, Z.; Liu, M.; Chang, J.; Wu, C. Preparation of copper-containing bioactive glass/eggshell membrane nanocomposites for improving angiogenesis, antibacterial activity and wound healing. *Acta Biomater.* **2016**, *36*, 254–266. [CrossRef]

48. Matsumoto, N.; Sato, K.; Yoshida, K.; Hashimoto, K.; Toda, Y. Preparation and characterization of β-tricalcium phosphate Co-doped with monovalent and divalent antibacterial metal ions. *Acta Biomater.* **2009**, *5*, 3157–3164. [CrossRef]

49. Zhang, X.; Huang, X.; Ma, Y.; Lin, N.; Fan, A.; Tang, B. Bactericidal behavior of Cu-containing stainless steel surfaces. *Appl. Surf. Sci.* **2012**, *258*, 10058–10063. [CrossRef]

50. Ruparelia, J.P.; Chatterjee, A.K.; Duttagupta, S.P.; Mukherji, S. Strain specificity in antimicrobial activity of silver and copper nanoparticles. *Acta Biomater.* **2008**, *4*, 707–716. [CrossRef]

51. Huang, Q.; Liu, X.; Zhang, R.; Yang, X.; Lan, C.; Feng, Q.; Liu, Y. The development of Cu-incorporated micro/nano-topographical bio-ceramic coatings for enhanced osteoblast response. *Appl. Surf. Sci.* **2019**, *465*, 575–583. [CrossRef]

52. Zhu, W.; Zhang, Z.X.; Gu, B.B.; Sun, J.Y.; Zhu, L.X. Biological activity and antibacterial property of nano-structured TiO$_2$ coating incorporated with Cu prepared by micro-arc oxidation. *J. Mater. Sci. Technol.* **2013**, *29*, 237–244. [CrossRef]

53. Zhang, X.; Li, J.; Wang, X.; Wang, Y.; Hang, R.; Huang, X.; Tang, B.; Chu, P.K. Effects of copper nanoparticles in porous TiO$_2$ coatings on bacterial resistance and cytocompatibility of osteoblasts and endothelial cells. *Mater. Sci. Eng. C* **2018**, *82*, 110–120. [CrossRef] [PubMed]

54. Huang, Q.; Li, X.; Elkhooly, T.A.; Liu, X.; Zhang, R.; Wu, H.; Feng, Q.; Liu, Y. The Cu-containing TiO$_2$ coatings with modulatory effects on macrophage polarization and bactericidal capacity prepared by micro-arc oxidation on titanium substrates. *Colloids Surf. B Biointerfaces* **2018**, *170*, 242–250. [CrossRef] [PubMed]

55. Zhang, L.; Guo, J.Q.; Huang, X.Y.; Zhang, Y.N.; Han, Y. The dual function of Cu-doped TiO$_2$ coatings on titanium for application in percutaneous implants. *J. Mater. Chem. B* **2016**, *4*, 3788–3800. [CrossRef]

56. Wu, H.B.; Zhang, X.Y.; Geng, Z.H.; Yin, Y.; Hang, R.Q.; Huang, X.B.; Yao, X.H.; Tang, B. Preparation, antibacterial effects and corrosion resistant of porous Cu-TiO$_2$ coatings. *Appl. Surf. Sci.* **2014**, *308*, 43–49. [CrossRef]

57. Kokubo, T.; Takadama, H. How useful is SBF in predicting in vivo bone bioactivity? *Biomaterials* **2006**, *27*, 2907–2915. [CrossRef] [PubMed]

58. Wang, Y.M.; Jiang, B.L.; Lei, T.Q.; Guo, L.X. Dependence of growth features of microarc oxidation coatings of titanium alloy on control modes of alternate pulse. *Mater. Lett.* **2004**, *58*, 1907–1911. [CrossRef]

59. Hanaor, D.A.H.; Sorrell, C.C. Review of the anatase to rutile phase transformation. *J. Mater. Sci.* **2011**, *46*, 855–874. [CrossRef]

60. Yerokhin, A.L.; Nie, X.; Leyland, A.; Matthews, A. Characterisation of oxide films produced by plasma electrolytic oxidation of a Ti–6Al–4V alloy. *Surf. Coat. Technol.* **2000**, *130*, 195–206. [CrossRef]

61. Li, Z.W.; Di, S.C. Microstructure and properties of MAO composite coatings containing nanorutile TiO$_2$ particles. *Surf. Rev. Lett.* **2017**, *24*, 1750115. [CrossRef]

62. Yerokhin, L.; Snizhko, L.O.; Gurevina, N.L.; Leyland, A.; Pilkington, A.; Matthews, A. Discharge characterization in plasma electrolytic oxidation of aluminium. *J. Phys. D-Appl. Phys.* **2003**, *36*, 2110–2120. [CrossRef]

63. Cimenoglu, H.; Gunyuz, M.; Kose, G.T.; Baydogan, M.; Ugurlu, F.; Sener, C. Micro-arc oxidation of Ti6Al4V and Ti6Al7Nb alloys for biomedical applications. *Mater. Charact.* **2011**, *62*, 304–311. [CrossRef]

64. Deng, F.L.; Zhang, W.Z.; Zhang, P.F.; Liu, C.H.; Ling, J.Q. Improvement in the morphology of micro-arc oxidised titanium surfaces: A new process to increase osteoblast response. *Mater. Sci. Eng. C-Mater. Boil. Appl.* **2010**, *30*, 141–147. [CrossRef]

65. Zhang, Z.X.; Sun, J.Y.; Hu, H.J.; Wang, Q.M.; Liu, X.Y. Osteoblast-like cell adhesion on porous silicon-incorporated TiO$_2$ coating prepared by micro-arc oxidation. *J. Biomed. Mater. Res. Part B-Appl. Biomater.* **2011**, *97B*, 224–234. [CrossRef] [PubMed]

66. Durdu, S.; Aktug, S.L.; Aktas, S.; Yalcin, E.; Usta, M. Fabrication and in vitro properties of zinc-based superhydrophilic bioceramic coatings on zirconium. *Surf. Coat. Technol.* **2018**, *344*, 467–478. [CrossRef]

67. Durdu, S.; Aktug, S.L.; Aktas, S.; Yalcin, E.; Cavusoglu, K.; Altinkok, A.; Usta, M. Characterization and in vitro properties of anti-bacterial Ag-based bioceramic coatings formed on zirconium by micro arc oxidation and thermal evaporation. *Surf. Coat. Technol.* **2017**, *331*, 107–115. [CrossRef]

68. Li, Y.D.; Wang, W.Q.; Duan, J.T.; Qi, M. A super-hydrophilic coating with a macro/micro/nano triple hierarchical structure on titanium by two-step micro-arc oxidation treatment for biomedical applications. *Surf. Coat. Technol.* **2017**, *311*, 1–9. [CrossRef]

69. Tang, W.X.; Yan, J.K.; Yang, G.; Gan, G.Y.; Du, J.H.; Zhang, J.M.; Liu, Y.C.; Shi, Z.; Yu, J.H. Effect of electrolytic solution concentrations on surface hydrophilicity of micro-arc oxidation ceramic film based on Ti6Al4V titanium alloy. *Rare Met. Mater. Eng.* **2014**, *43*, 2883–2888.

70. Zhang, Y.M.; Bataillon-Linez, P.; Huang, P.; Zhao, Y.M.; Han, Y.; Traisnel, M.; Xu, K.W.; Hildebrand, H.F. Surface analyses of micro-arc oxidized and hydrothermally treated titanium and effect on osteoblast behavior. *J. Biomed. Mater. Res. Part A* **2004**, *68A*, 383–391. [CrossRef] [PubMed]

71. Das, K.; Bose, S.; Bandyopadhyay, A. Surface modifications and cell–materials interactions with anodized Ti. *Acta Biomater.* **2007**, *3*, 573–585. [CrossRef] [PubMed]

72. Wang, Z.W.; Li, Q.; She, Z.X.; Chen, F.N.; Li, L.Q.; Zhang, X.X.; Zhang, P. Facile and fast fabrication of superhydrophobic surface on magnesium alloy. *Appl. Surf. Sci.* **2013**, *271*, 182–192. [CrossRef]

73. Wang, P.; Zhang, D.; Qiu, R.; Wan, Y.; Wu, J.J. Green approach to fabrication of a super-hydrophobic film on copper and the consequent corrosion resistance. *Corros. Sci.* **2014**, *80*, 366–373. [CrossRef]

74. Cui, X.J.; Lin, X.Z.; Liu, C.H.; Yang, R.S.; Zheng, X.W.; Gong, M. Fabrication and corrosion resistance of a hydrophobic micro-arc oxidation coating on AZ31 Mg alloy. *Corros. Sci.* **2015**, *90*, 402–412. [CrossRef]

75. Bayati, M.R.; Molaei, R.; Kajbafvala, A.; Zanganeh, S.; Zargar, H.R.; Janghorban, K. Investigation on hydrophilicity of micro-arc oxidized TiO$_2$ nano/micro-porous layers. *Electrochim. Acta* **2010**, *55*, 5786–5792. [CrossRef]

76. Pereira, M.M.; Kurnia, K.A.; Sousa, F.L.; Silva, N.J.O.; Lopes-da-Silva, J.A.; Coutinhoa, J.A.P.; Freire, M.G. Contact angles and wettability of ionic liquids on polar and non-polar surfaces. *Phys. Chem. Chem. Phys.* **2015**, *17*, 31653–31661. [CrossRef]

77. Kokubo, T. Bioactive glass ceramics: Properties and applications. *Biomaterials* **1991**, *12*, 155–163. [CrossRef]

78. Leon, A.; Reuquen, P.; Garin, C.; Segura, R.; Vargas, P.; Zapata, P.; Orihuela, P.A. FTIR and raman characterization of TiO$_2$ nanoparticles coated with polyethylene glycol as carrier for 2-methoxyestradiol. *Appl. Sci.* **2017**, *7*, 49. [CrossRef]

79. Chellappa, M.; Anjaneyulu, U.; Manivasagam, G.; Vijayalakshmi, U. Preparation and evaluation of the cytotoxic nature of TiO$_2$ nanoparticles by direct contact method. *Int. J. Nanomed.* **2015**, *10*, 31–41.

80. Khan, M.; Naqvi, A.H.; Ahmad, M. Comparative study of the cytotoxic and genotoxic potentials of zinc oxide and titanium dioxide nanoparticles. *Toxicol. Rep.* **2015**, *2*, 765–774. [CrossRef]

81. Ślósarczyk, A.; Paszkiewicz, Z.; Paluszkiewicz, C. FTIR and XRD evaluation of carbonated hydroxyapatite powders synthesized by wet methods. *J. Mol. Struct.* **2005**, *744–747*, 657–661.

82. Rapacz-Kmita, A.; Paluszkiewicz, C.; Ślósarczyk, A.; Paszkiewicz, Z. FTIR and XRD investigations on the thermal stability of hydroxyapatite during hot pressing and pressureless sintering processes. *J. Mol. Struct.* **2005**, *744–747*, 653–656. [CrossRef]

83. Nayak, Y.; Rana, R.; Pratihar, S.; Bhattacharyya, S. Low-temperature processing of dense hydroxyapatite–zirconia composites. *Int. J. Appl. Ceram. Technol.* **2008**, *5*, 29–36. [CrossRef]

84. Kim, H.-W.; Noh, Y.-J.; Koh, Y.-H.; Kim, H.-E.; Kim, H.-M. Effect of CaF$_2$ on densification and properties of hydroxyapatite–zirconia composites for biomedical applications. *Biomaterials* **2002**, *23*, 4113–4121. [CrossRef]

85. Basar, B.; Tezcaner, A.; Keskin, D.; Evis, Z. Improvements in microstructural, mechanical, and biocompatibility properties of nano-sized hydroxyapatites doped with yttrium and fluoride. *Ceram. Int.* **2010**, *36*, 1633–1643. [CrossRef]

86. Rintoul, L.; Byrne, E.W.; Suzuki, S.; Grondahl, L. FT–IR spectroscopy fluoro–substituted hydroxyapatite: Strengths and limitations. *J. Mater. Sci. Mater. Med.* **2007**, *18*, 1701–1709. [CrossRef]

87. Aykul, A. Investigation of Effect of Yttrium Fluoride on Microstructural and Mechanical Properties of Hydroxyapatite and Partially Stabilized Zirconia Composites. Master's Thesis, Gebze Institute of Technology, Gebze, Turkey, January 2010.

88. Aktuğ, S.L.; Durdu, S.; Yalçın, E.; Çavuşoğlu, K.; Usta, M. Bioactivity and biocompatibility of hydroxyapatite-based bioceramic coatings on zirconium by plasma electrolytic oxidation. *Mater. Sci. Eng. C* **2017**, *71*, 1020–1027. [CrossRef]

89. Aktuğ, S.L.; Durdu, S.; Yalçın, E.; Çavuşoğlu, K.; Usta, M. In vitro properties of bioceramic coatings produced on zirconium by plasma electrolytic oxidation. *Surf. Coat. Technol.* **2017**, *324*, 129–139. [CrossRef]

90. Durdu, S.; Deniz, Ö.F.; Kutbay, I.; Usta, M. Characterization and formation of hydroxyapatite on Ti6Al4V coated by plasma electrolytic oxidation. *J. Alloy. Compd.* **2013**, *551*, 422–429. [CrossRef]

91. Pecheva, E.V.; Pramatarova, L.D.; Maitz, M.F.; Pham, M.T.; Kondyuirin, A.V. Kinetics of hydroxyapatite deposition on solid substrates modified by sequential implantation of Ca and P ions—Part I. FTIR and raman spectroscopy study. *Appl. Surf. Sci.* **2004**, *235*, 176–181. [CrossRef]

92. Shaltout, A.A.; Allam, M.A.; Moharram, M.A. FTIR spectroscopic, thermal and xrd characterization of hydroxyapatite from new natural sources. *Spectrochim. Acta Part A-Mol. Biomol. Spectrosc.* **2011**, *83*, 56–60. [CrossRef] [PubMed]

93. Meskinfam, M.; Sadjadi, M.; Jazdarreh, H. Synthesis and characterization of surface functionalized nanobiocomposite by nano hydroxyapatite. *Int. J. Mater. Metall. Eng.* **2012**, *6*, 192–195.

94. Aktug, S.L.; Kutbay, I.; Usta, M. Characterization and formation of bioactive hydroxyapatite coating on commercially pure zirconium by micro arc oxidation. *J. Alloy. Compd.* **2017**, *695*, 998–1004. [CrossRef]

95. Müller, L.; Müller, F.A. Preparation of SBF with different content and its influence on the composition of biomimetic apatites. *Acta Biomater.* **2006**, *2*, 181–189. [CrossRef] [PubMed]

96. Li, H.; Khor, K.A.; Cheang, P. Properties of heat-treated calcium phosphate coatings deposited by high-velocity oxy-fuel (hvof) spray. *Biomaterials* **2002**, *23*, 2105–2112. [CrossRef]

97. Song, W.H.; Jun, Y.K.; Han, Y.; Hong, S.H. Biomimetic apatite coatings on micro-arc oxidized titania. *Biomaterials* **2004**, *25*, 3341–3349. [CrossRef]

98. Li, P.J.; Kangasniemi, I.; Degroot, K.; Kokubo, T. Bonelike hydroxyapatite induction by a gel-derived titania on a titanium substrate. *J. Am. Ceram. Soc.* **1994**, *77*, 1307–1312. [CrossRef]

99. Hu, C.H.; Xia, M.S. Adsorption and antibacterial effect of copper-exchanged montmorillonite on *escherichia coli* k-88. *Appl. Clay Sci.* **2006**, *31*, 180–184. [CrossRef]

100. Ohsumi, Y.; Kitamoto, K.; Anraku, Y. Changes induced in the permeability barrier of the yeast plasma-membrane by cupric ion. *J. Bacteriol.* **1988**, *170*, 2676–2682. [CrossRef]

101. Dan, Z.G.; Ni, H.W.; Xu, B.F.; Xiong, J.; Xiong, P.Y. Microstructure and antibacterial properties of AISI 420 stainless steel implanted by copper ions. *Thin Solid Films* **2005**, *492*, 93–100. [CrossRef]

102. Theivasanthi, T.; Alagar, M. Studies of copper nanoparticles effects on micro-organisms. *Ann. Biol. Res.* **2011**, *2*, 368–373.

103. Ramyadevi, J.; Jeyasubramanian, K.; Marikani, A.; Rajakumar, G.; Rahuman, A.A. Synthesis and antimicrobial activity of copper nanoparticles. *Mater. Lett.* **2012**, *71*, 114–116. [CrossRef]

104. Trapalis, C.C.; Kokkoris, M.; Perdikakis, G.; Kordas, G. Study of antibacterial composite Cu/SiO$_2$ thin coatings. *J. Sol-Gel Sci. Technol.* **2003**, *26*, 1213–1218. [CrossRef]

105. Wang, Q.; Larese-Casanova, P.; Webster, T.J. Inhibition of various gram-positive and gram-negative bacteria growth on selenium nanoparticle coated paper towels. *Int. J. Nanomed.* **2015**, *10*, 2885–2894.